

Supplementary Information

The proline-rich antimicrobial peptide Api137 disrupts large ribosomal subunit assembly and induces misfolding

Simon M. Lauer^{1,2,#}, Jakob Gasse^{3,4,#}, Andor Krizsan^{3,4}, Maren Reepmeyer^{3,4}, Thiemo Sprink^{5,6}, Rainer Nikolay^{1,7}✉, Christian M. T. Spahn¹✉, and Ralf Hoffmann^{3,4}✉.

authors contributed equally and thus both have the right to use their names on the first place

✉ Corresponding authors: Dr. Rainer Nikolay (nikolay@molgen.mpg.de), Prof. Christian M. T. Spahn (christian.spahn@charite.de) and Prof. Ralf Hoffmann (bioanaly@rz.uni-leipzig.de)

Affiliation:

¹Institut für Medizinische Physik und Biophysik, Charité - Universitätsmedizin Berlin, corporate member of Freie Universität Berlin and Humboldt Universität zu Berlin, Berlin, Germany.

²Humboldt-Universität zu Berlin, Institut für Biologie, 10099 Berlin, Germany

³Institute of Bioanalytical Chemistry, Faculty of Chemistry and Mineralogy, Universität Leipzig, Leipzig, Germany.

⁴Center for Biotechnology and Biomedicine, Universität Leipzig, Leipzig, Germany.

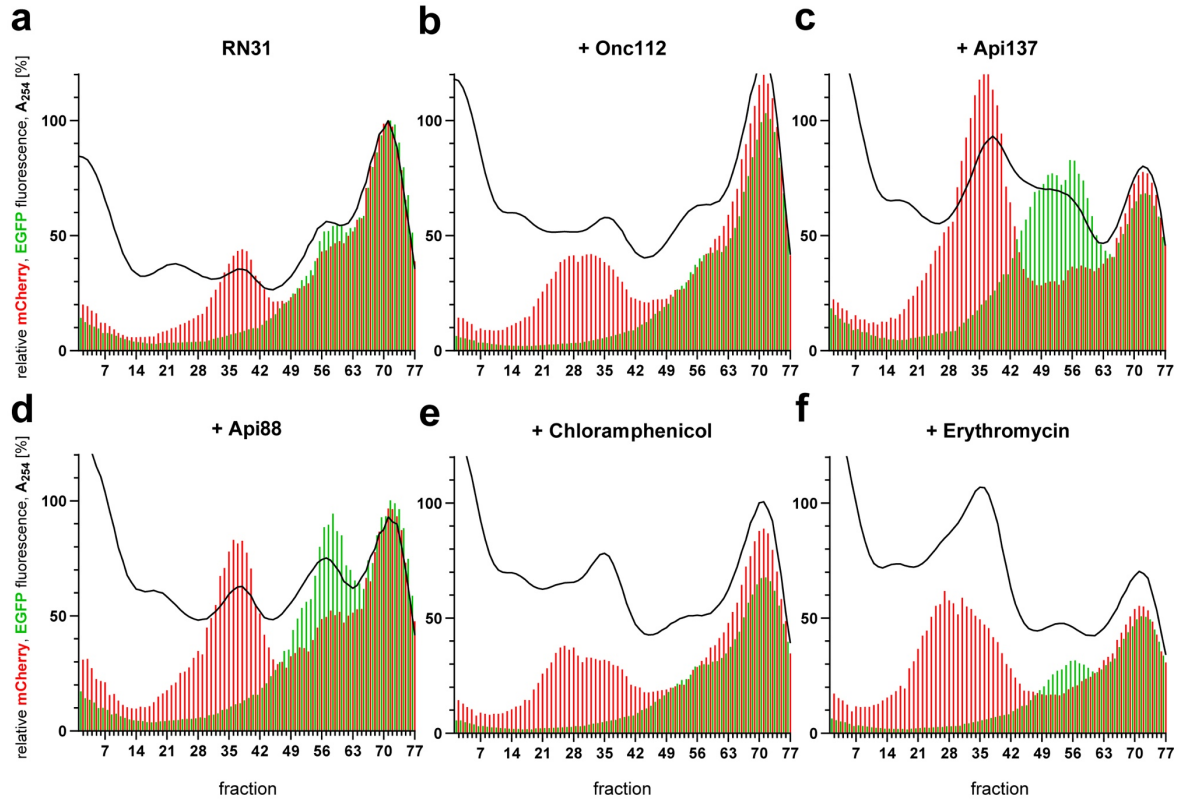
⁵Core Facility for Cryo-Electron Microscopy, Charité - Universitätsmedizin Berlin, Berlin, Germany

⁶Cryo-EM Facility, Max Delbrück Center for Molecular Medicine in the Helmholtz Association, Berlin, Germany

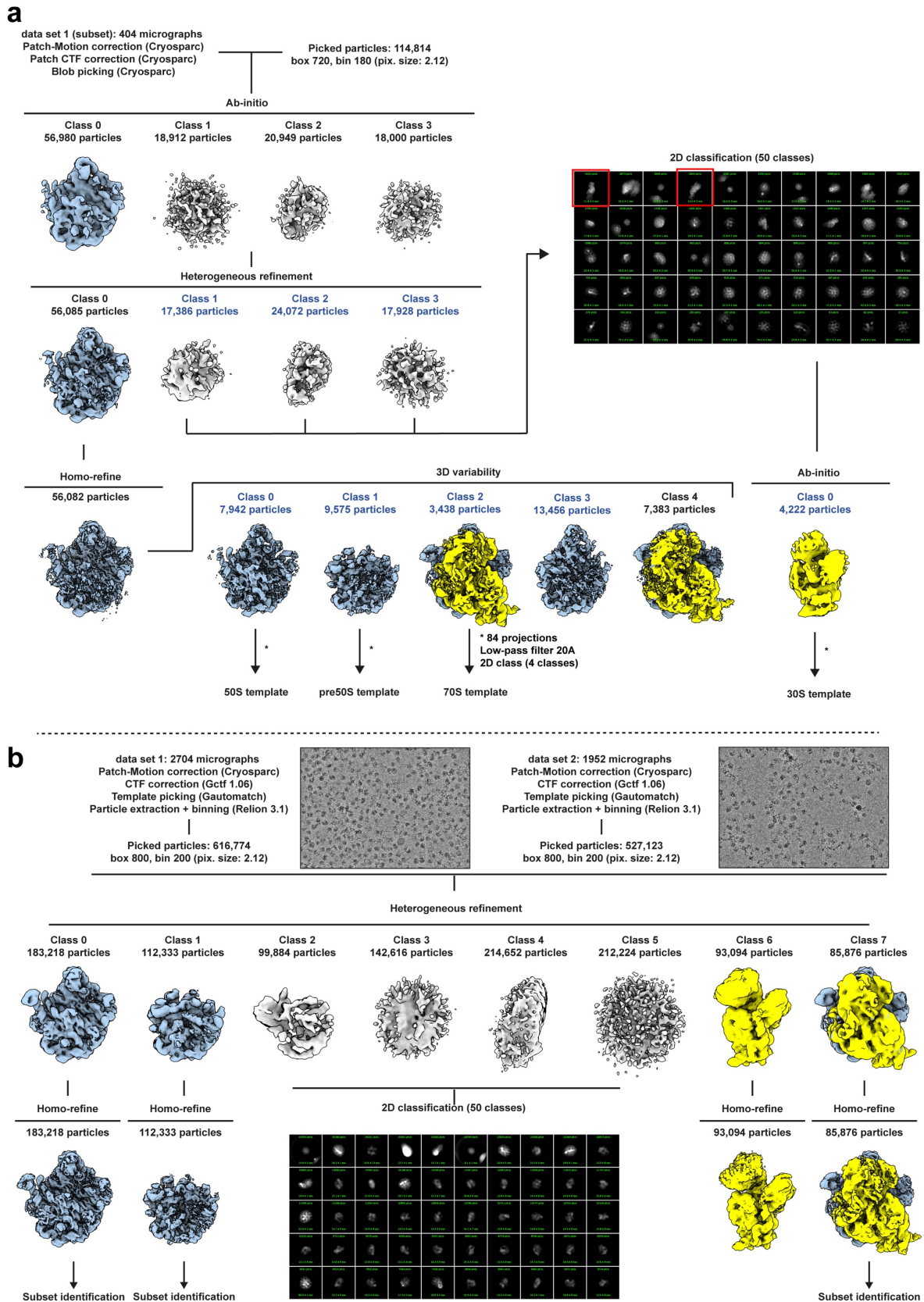
⁷Department of Genome Regulation, Max Planck Institute for Molecular Genetics, Berlin, Germany.

Table of contents

Supplementary Fig. 1: Ribosome profile analysis of <i>E. coli</i> RN31 in the presence of Onc112, Api137, Api88, Chloramphenicol and Erythromycin	3
Supplementary Fig. 2: Initial class identification and alignment	4
Supplementary Fig. 3: Identification of subclasses in Api137 treated samples	6
Supplementary Fig. 4: Sorting scheme of control data set	8
Supplementary Fig. 5: Cryo-EM maps, models, RNA composition, local resolutions and Model-map fits identified precursors	9
Supplementary Fig. 6: Global FSC curves and angular distribution plots of Api137-precursor maps	12
Supplementary Fig. 7: Comparison with <i>in vitro</i> reconstituted pre-50S states	14
Supplementary Fig. 8: All late precursors show incorporated uL22	15
Supplementary Fig. 9: Structures of pre-50S intermediates suggesting delayed and rerouted assembly pathways upon Api137 treatment	16
Supplementary Fig. 10: Sorting scheme of the particles from Api137-treated cells in the presence of 30 μ M Api137.....	18
Supplementary Fig. 11: Cryo-EM maps, models, local and global resolutions and angular distributions of pooled refinements of Api137-precursors in the presence of 30 μ M Api137.....	22
Supplementary Fig. 12: Absence and presence of Api137 at the PET binding site	24
Supplementary Fig. 13: Api137 binding to pre-50S precursors and 50S at the PET exit binding site.....	26
Supplementary Tab. 1: Cryo-EM data collection, refinement, and validation statistics for the control data set	28
Supplementary Tab. 2: Cryo-EM data collection, refinement, and validation statistics for the data set from Api137-treated cells	29
Supplementary Tab. 3: Cryo-EM data collection, refinement, and validation statistics for the data set from Api137-treated cells supplemented with Api137... ..	31

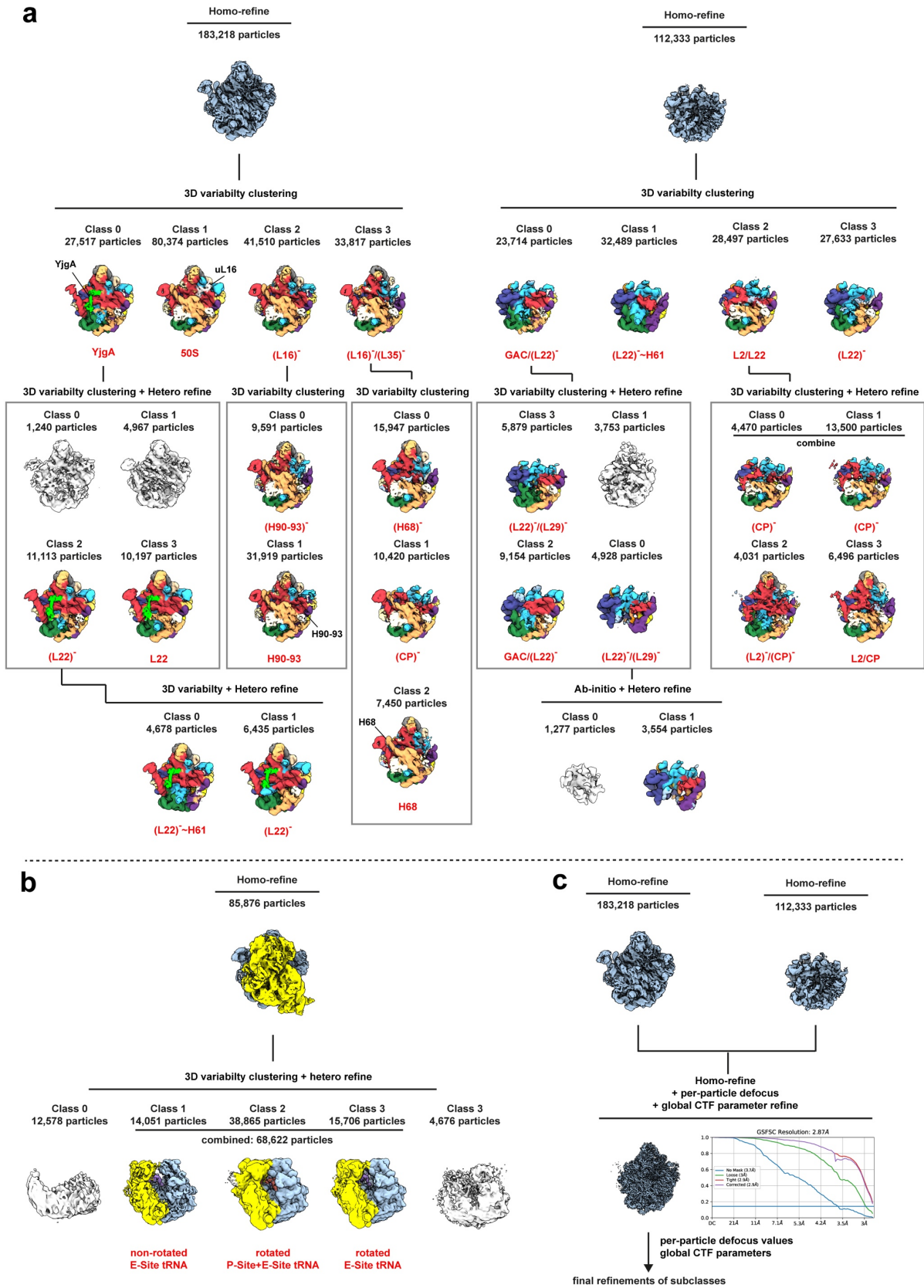


Supplementary Fig. 1 | Ribosome profile analysis of *E. coli* RN31 in the presence of Onc112, Api137, Api88, Chloramphenicol and Erythromycin. a - f All absorbance and fluorescence values were normalized to the mean value of the corresponding maximum peak intensity of the 70S fraction in the control. OD₂₅₄ (black curve) and EGFP and mCherry fluorescence values (green and red bars, respectively) obtained for **a** *E. coli* RN31 grown in culture medium (n = 10) and incubated with **b** Onc112 (8 μg/mL, n = 6), **c** Api137 (8 μg/mL, n = 10), **d** Api88 (8 μg/mL, n = 2), **e** chloramphenicol (8 μg/mL, n = 6) or **f** erythromycin (128 μg/mL, n = 6) along a sucrose gradient from 5 to 25%.



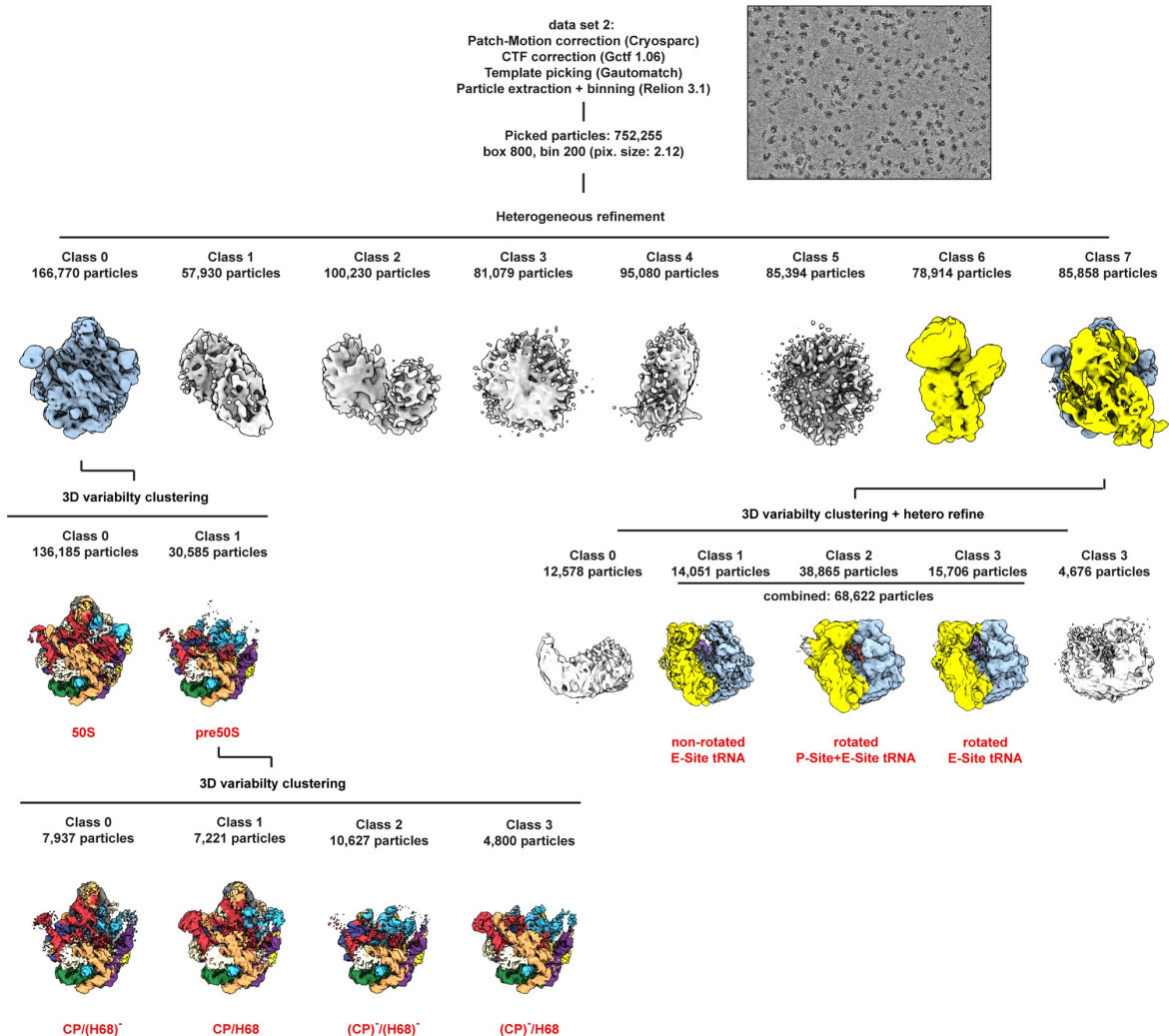
Supplementary Fig. 2 | Initial class identification and alignment. **a** A subset of data set 1 was pre-processed in CryoSPARC using patch-motion correction (standard parameters) and patch-CTF correction (resolution range: 12 Å - 4 Å). Particles were picked using a blob picker with a particle

diameter ranging from 140 to 220 Å. Particles were extracted with a box size of 720 Å and binned on-the-fly to 180 Å for an initial pixel size of 2.12 Å. Particles were subjected to one round of multi-class ab-initio reconstruction (class similarity = 0) for an initial consensus map, followed by heterogeneous refinement to discard non-ribosomal particles. A consensus refinement was performed on the ribosomal map, followed by a 3D variability analysis. The variability analysis revealed the presence of 70S, 50S and pre-50S classes. 30S was identified using a 2D classification, followed by selection of respective classes and template generation using ab-initio reconstruction. To improve particle picking, 84 equally spaced projections from each 3D volume (70S, 30S, 50S, pre-50S) were generated in CryoSPARC and filtered to 20 Å, followed by Xmipp3 2D classification (four classes for each set of 84 projections) to generate generalized picking templates. 2D classes were added to one stack for a final set of 16 picking templates. Particles were picked again, now using both datasets and the previously generated templates in Gautomatch (developed by K. Zhang). Particle images were extracted and normalized, using Relion 3.1⁴⁵ with a box size of 800 and Fourier cropped to 200 for sorting. **b** Newly extracted particles from both data sets were reassigned to the previously identified 70S, 50S, 30S and pre-50S states and non-ribosomal classes, followed by a homogenous refinement. Particles to be discarded were double-checked for remaining ribosomal particles using a 2D classification.

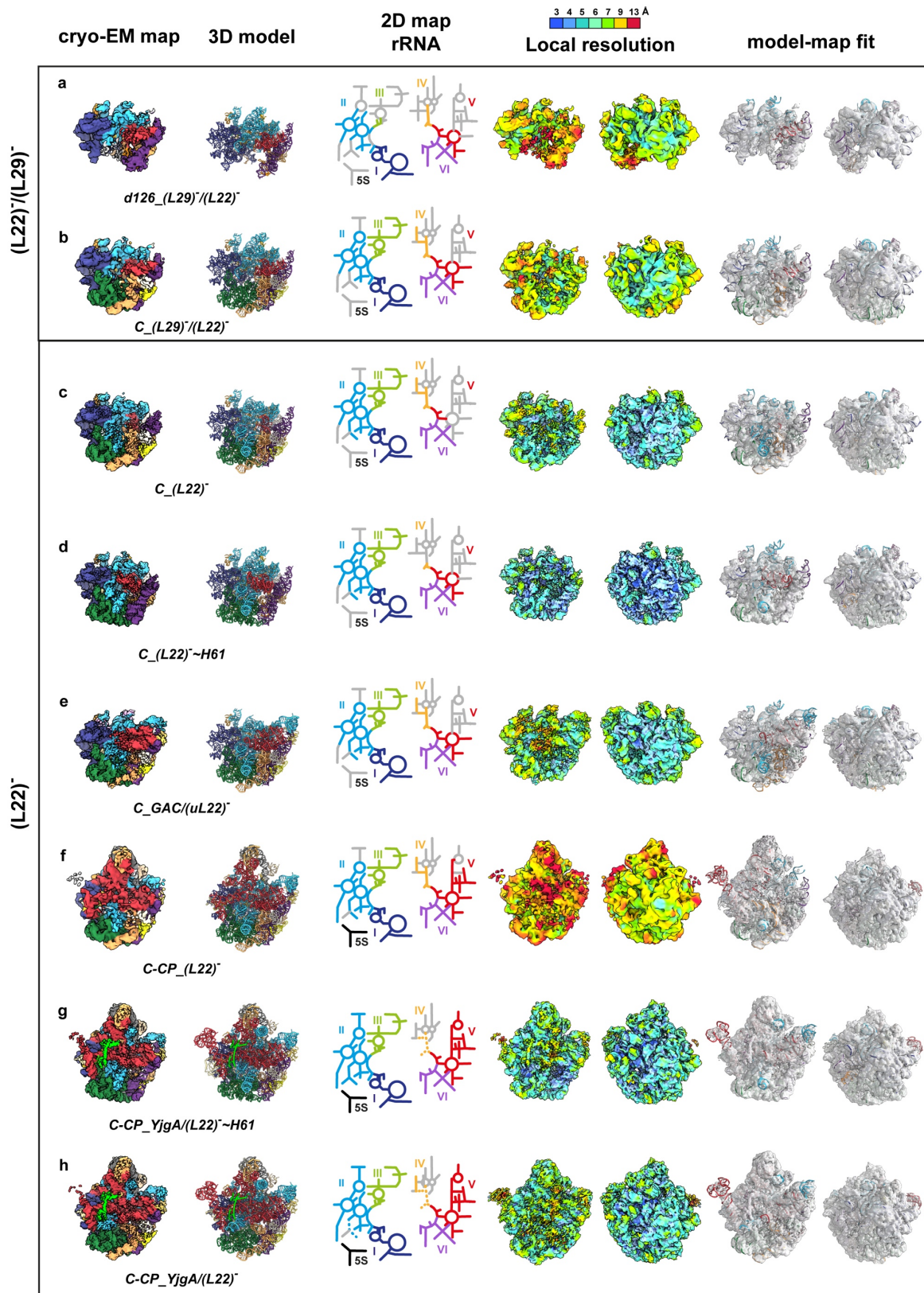


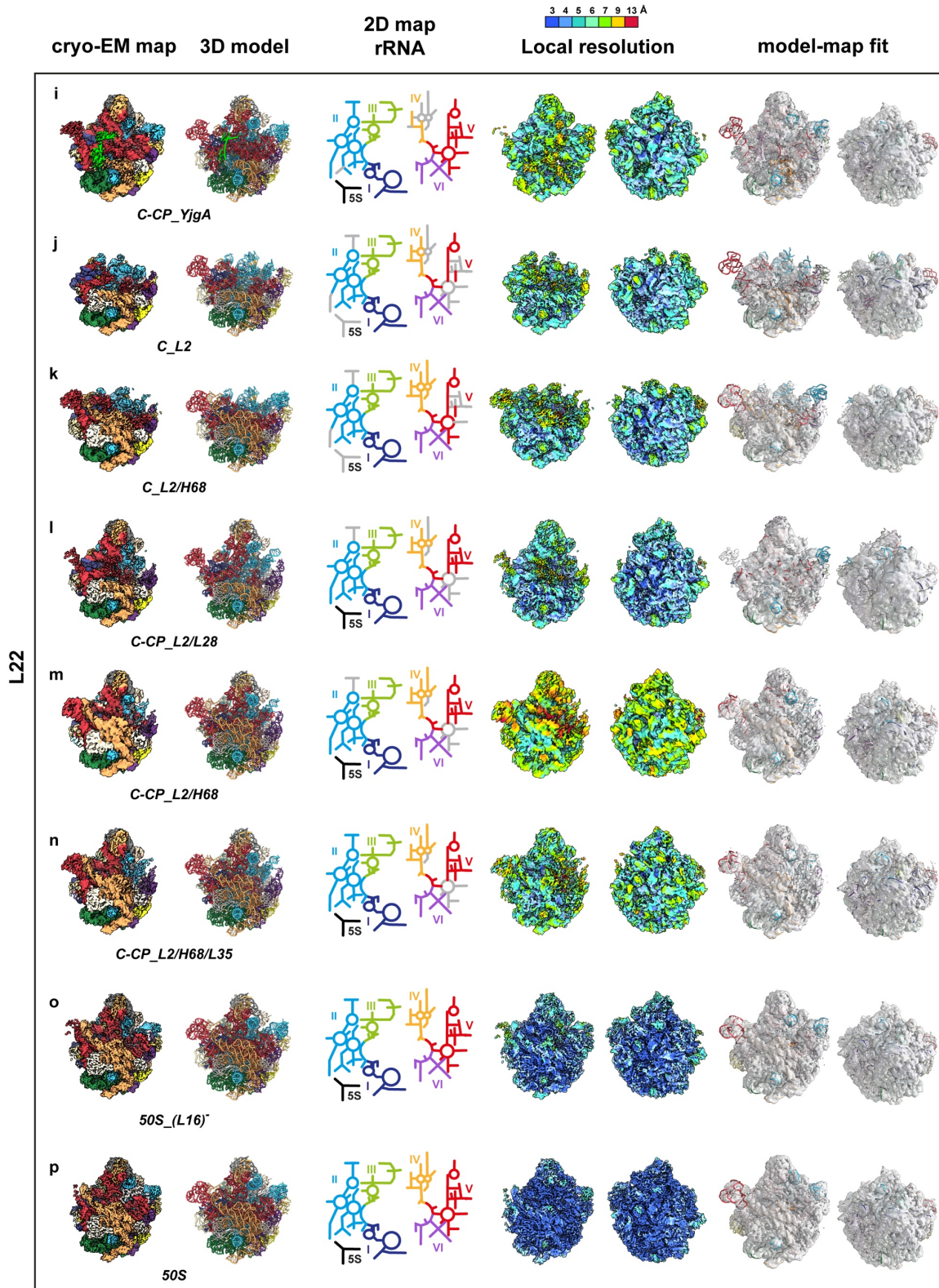
Supplementary Fig. 3 | Identification of subclasses in Api137 treated samples. a 50S and pre-50S states were subjected to multiple rounds of 3D variability analysis, until there was no more separation of distinct states. When denoted, clusters from 3D variability analyses were used in a Heterogenous

refinement for an additional re-assignment step. **b** Principle 70S states were identified using 3D variability analysis, followed by an additional Heterogenous refinement. Non-defined classes of 70S, 50S and pre-50S states were discarded. **c** To improve per-particle CTF values, 50S and pre-50S states were aligned to a single volume using an on-the-fly global and local CTF correction. Final refinements of distinct substrates were performed using optimized CTF values from this consensus refinement.



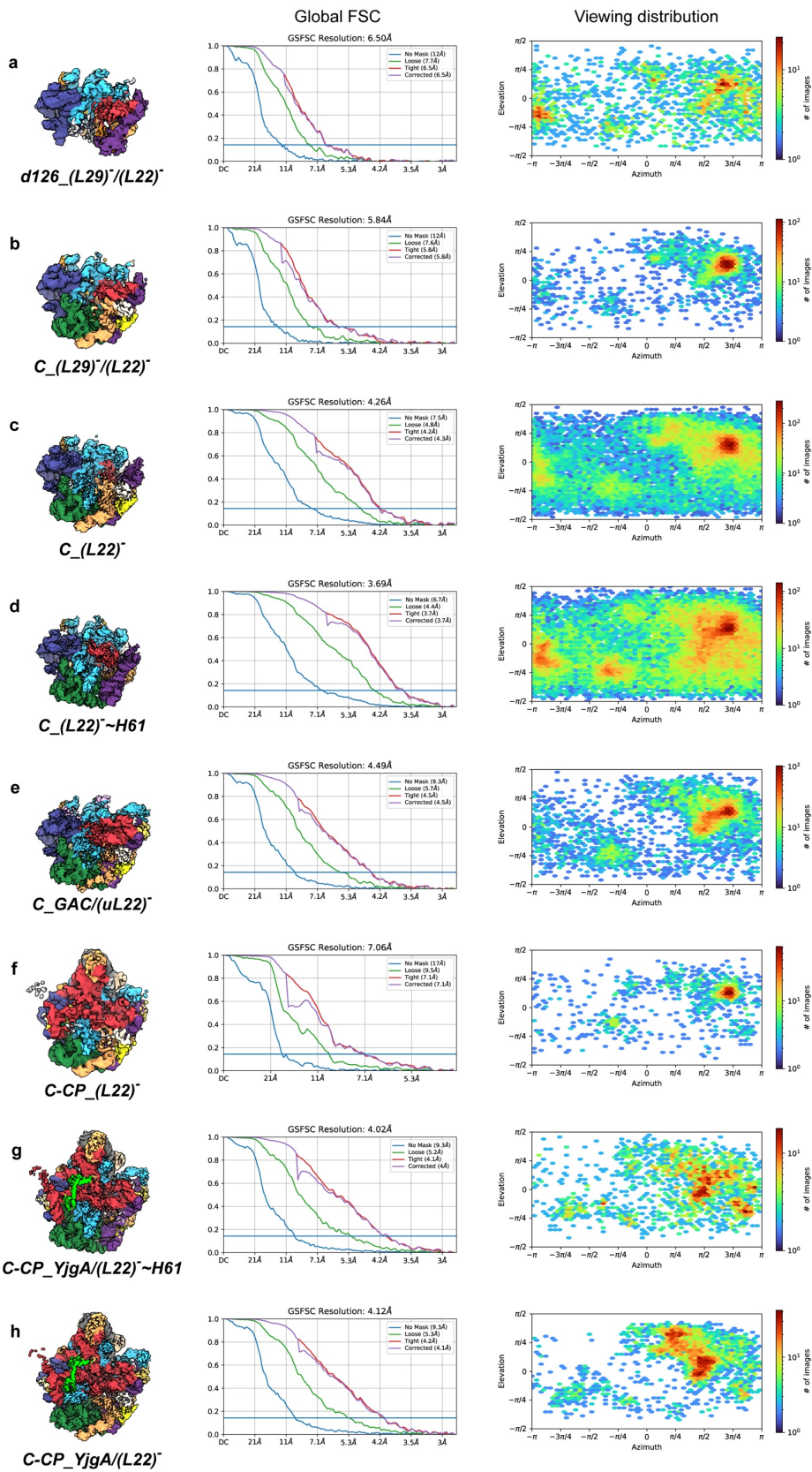
Supplementary Fig. 4 | Sorting scheme of control data set. The control data set was pre-processed in CryoSPARC using patch-motion correction (standard parameters) and patch-CTF correction (resolution range: 12 Å – 4 Å). Particles were picked using a blob picker with a particle diameter ranging from 140 to 220 Å. Particles were extracted with a box size of 720 Å and binned on-the-fly to 180 Å for an initial pixel size of 2.12 Å. Particles were subsequently assigned to the principal and non-ribosomal classes, identified in the Api137 data set. Particles corresponding to 50S, 30S, and 70S classes were refined once and subjected to 3D variability analysis until no more separation was observed.

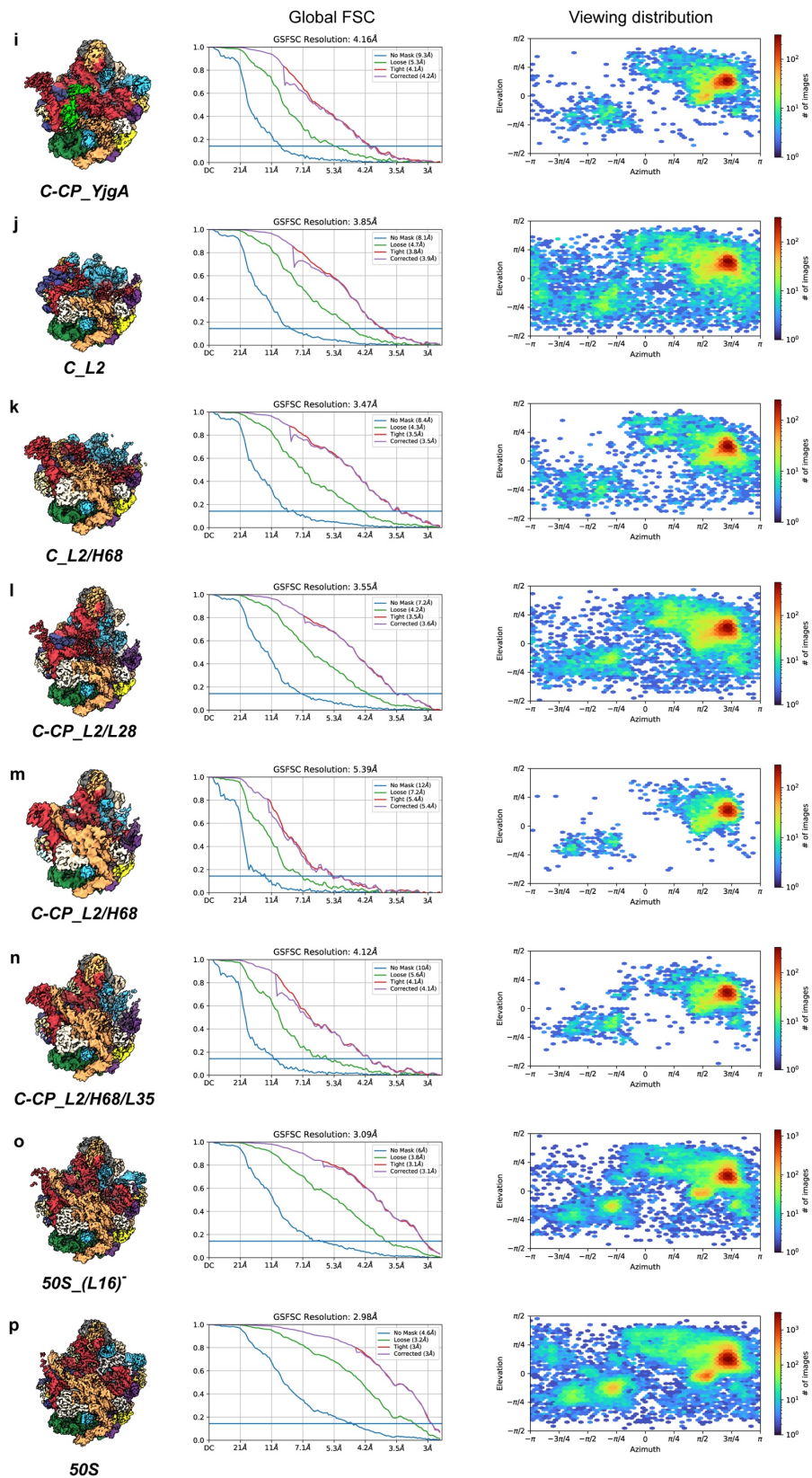




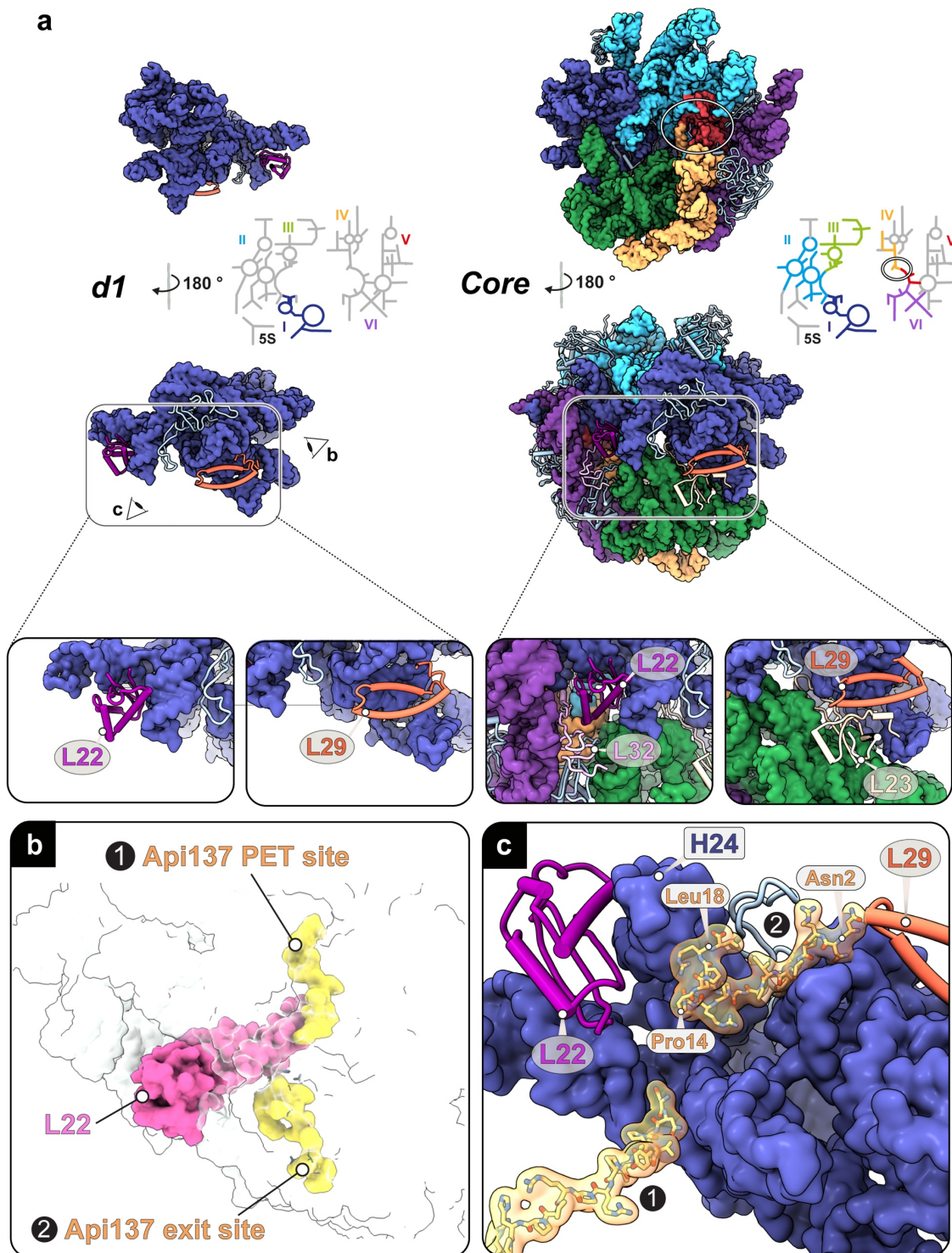
Supplementary Fig. 5 | cryo-EM maps, models, RNA composition, local resolutions and model-map fits of identified precursors. a-p States were lined up by their degree of structural completeness. Cryo-EM maps with rRNA and L-proteins color-coded according to the six architectural domains of the 23S rRNA they are part of. 3D PDB models, and 2D maps with the six rRNA domains color-coded. Colored regions indicate stably formed segments, for which cryo-EM densities were obtained.

Additionally, local resolutions (crown and back view) are shown for each state. 3D PDB models color-coded according to the six architectural domains of the 23S rRNA. Model-map fits show cryo-EM maps and models of all states a in crown and back view. Cryo-EM maps for this analysis were derived by subjecting final states to an additional ab-initio reconstruction, followed by Homogenous refinement, shown at a threshold of 0.33. Remaining heterogeneity in parts of the individual states is indicated in **bold**: **a** *d126_(L29)⁻/(L22)⁻*: (**uL6**, **bL30**), **b** *C_(L29)⁻/(L22)⁻* : (**uL6**, **bL30**), **c** *C_(L22)⁻*: (**H34**), **d** *C_(L22)⁻~H61*: (**bL30**), **e** *C_GAC(L22)⁻*: (**bL30**, **H34**, **H63**), **f** *C-CP_YjgA_(L22)⁻~H61*, **g** *C-CP_YjgA_(L22)⁻*, **h** *C-CP_YjgA: YjgA*, **i** *C_L2*: (**uL6**, **uL22**, **bL30**), **j** *C_H68*: (**uL6**, **bL30**, **H90-93**), **k** *C-CP_L2/L28*, **l** *C-CP_(L22)⁻*: (**uL22**), **m** *C-CP_H68*: (**H90-93**), **n** *C-CP_H68_L35*: (**H90-93**), **o** *50S_(L16)⁻*, **p** *50S*.



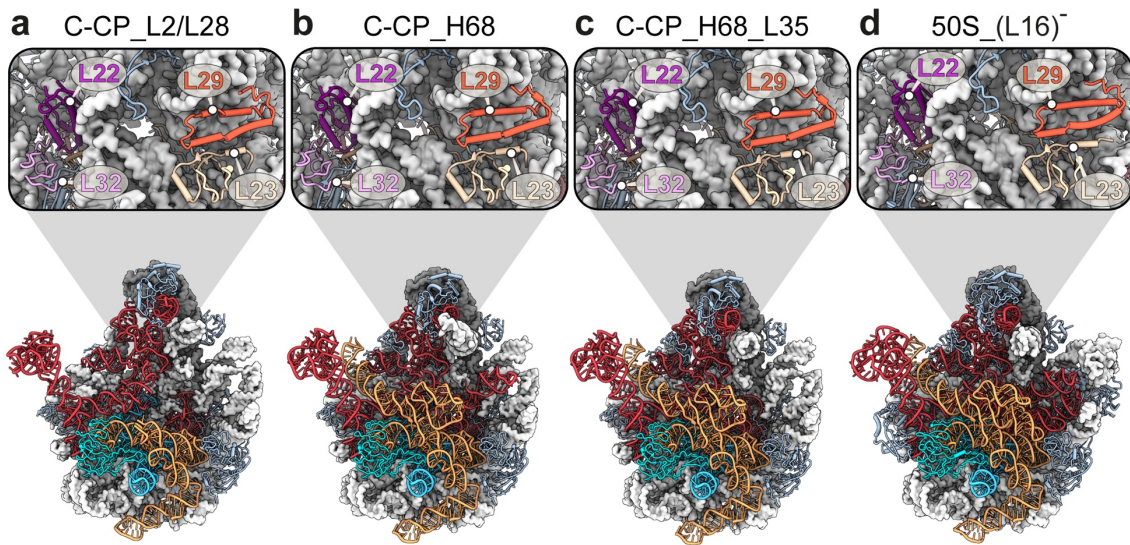


Supplementary Fig. 6 | Global FSC curves and angular distribution of pre-50S precursor maps. a-p Cryo-EM maps of all states are shown. For each state, the global Fourier-shell correlation (FSC) curves with estimated global resolutions at the 0.143 cut-off, as well as the angular distribution plots of the final reconstructions, are provided.

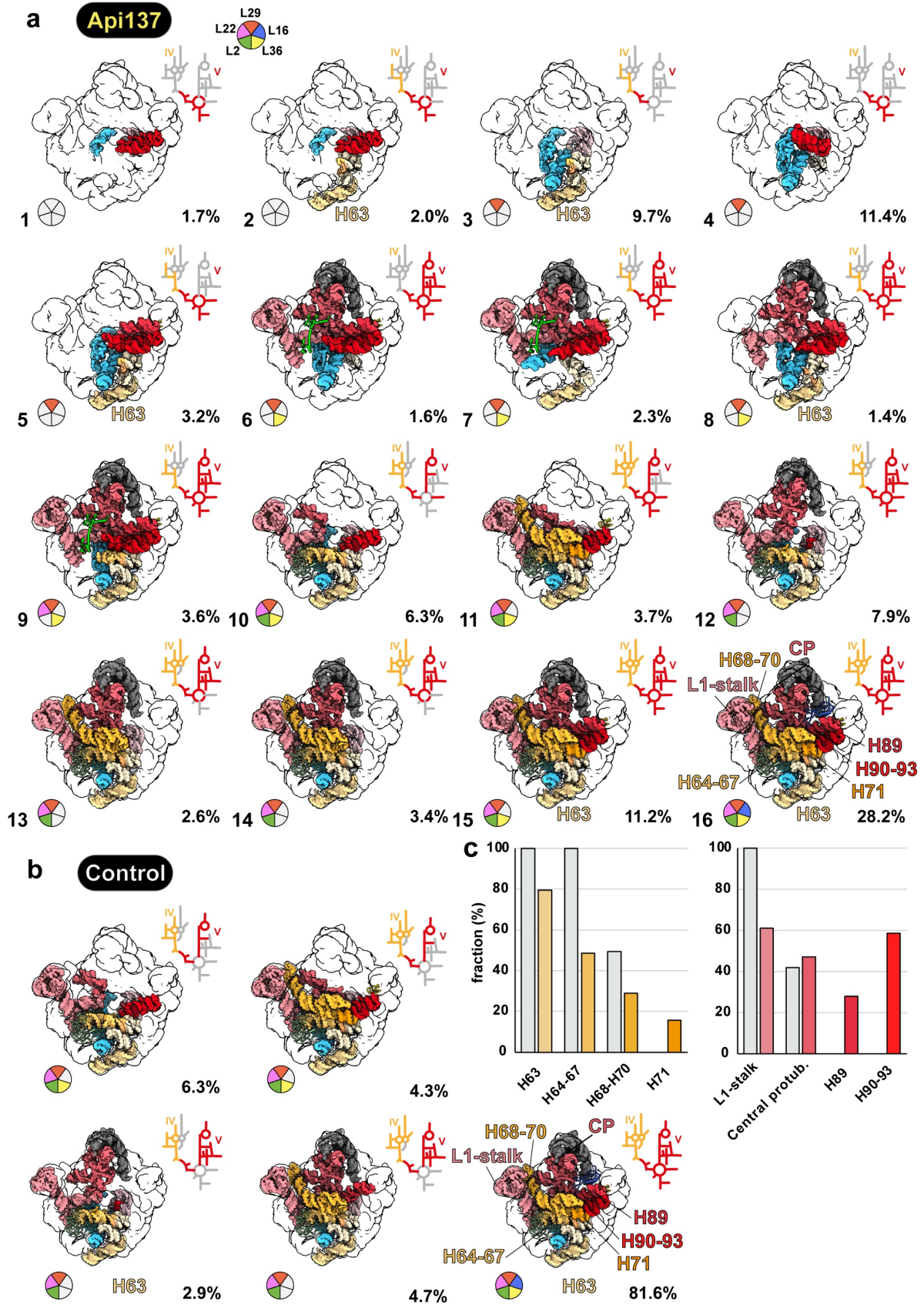


Supplementary Fig. 7 | Comparison with *in vitro* reconstituted pre-50S states. **a** Previously identified hallmark assembly states *d1* and *C* (core) are shown. Structures are shown as a surface model at 5 Å resolution and color-coded according to the 23S rRNA domain architecture. 2D plots show structured regions of the entire subunit. Enlargements show the positions of uL22, uL29, bL32, and bL23. Viewing angles in **b** and **c** are indicated using schematic eyes. **b** Previously identified positions of the PET and PET exit binding sites of Api137 (yellow) on the 50S subunit are shown relative to uL22 (pink). uL22 and Ap137 are shown as a surface models. **c** Atomic models and simulated densities at 4

Å resolution of both Api137 binding sites on the 50S subunit are superimposed on the assembly state *d1*. Maps and models in **a** and **b** taken from Lauer et al., 2024 (PDB: 8RPY).

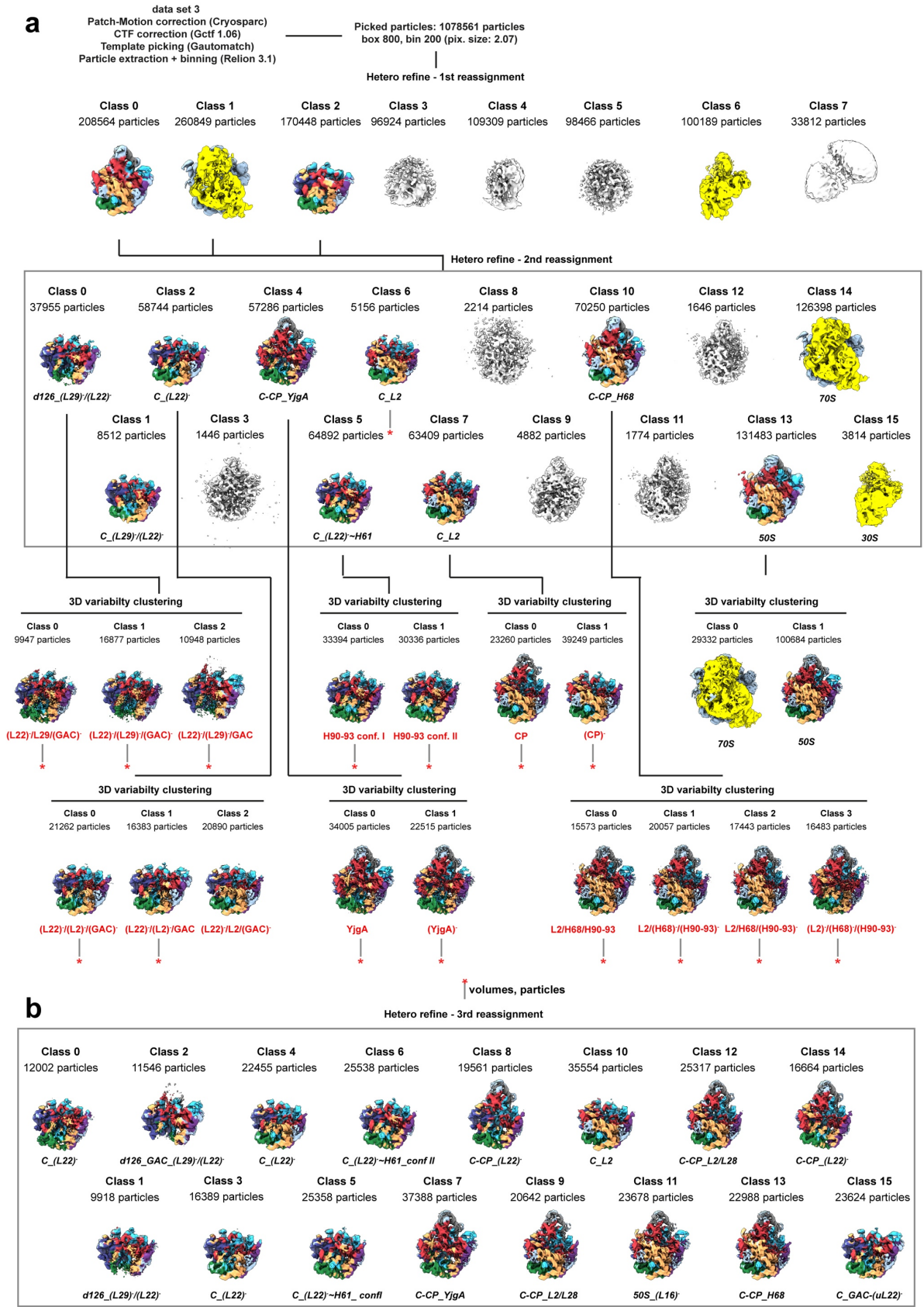


Supplementary Fig. 8 | All late precursors show incorporated uL22. Late assembly states identified in Api137 *ex vivo* precursors. Helix H34 and helices in domains IV and V are shown as ribbons, the remaining subunit is shown as a surface model at 5 Å resolution.

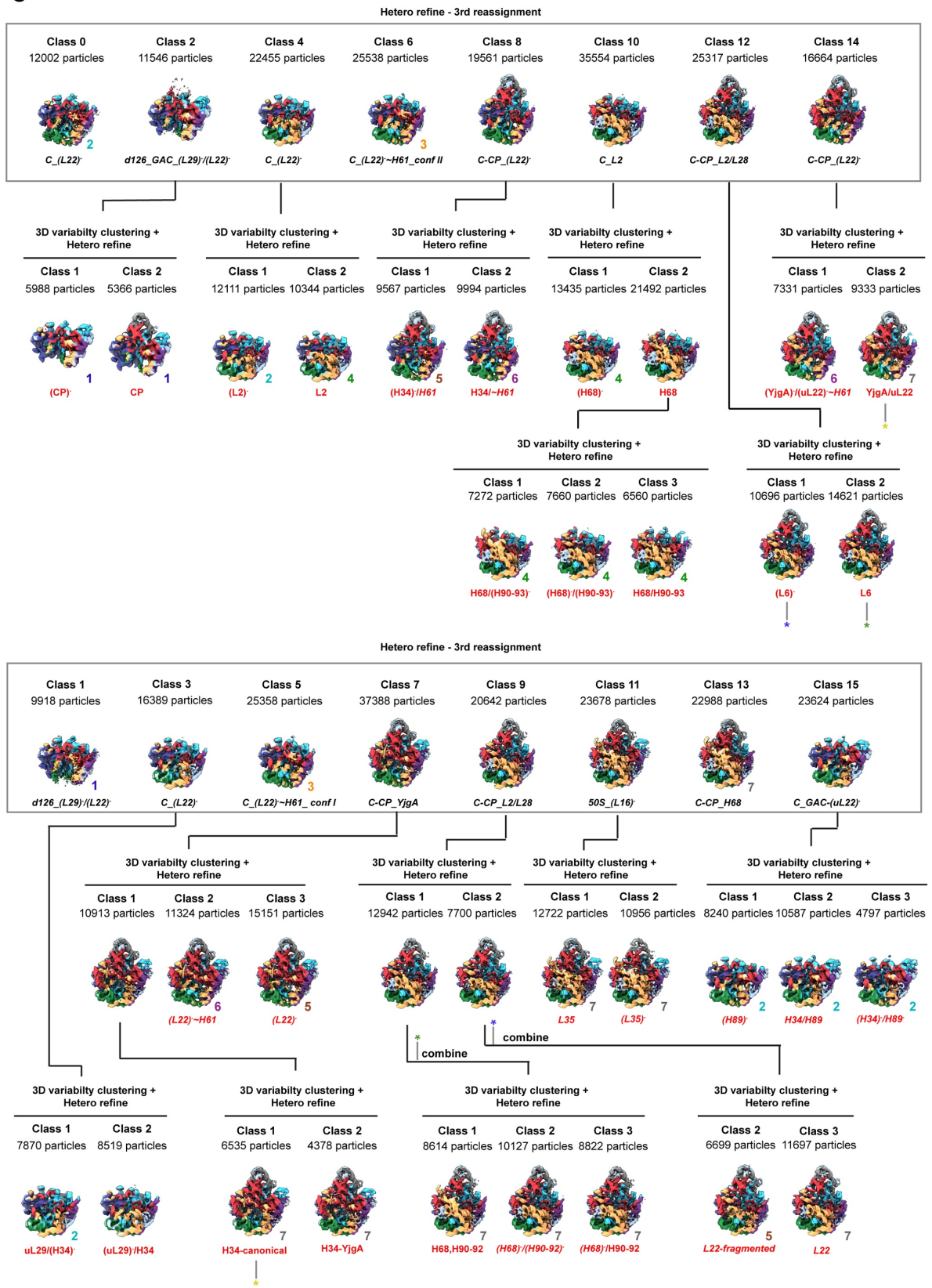


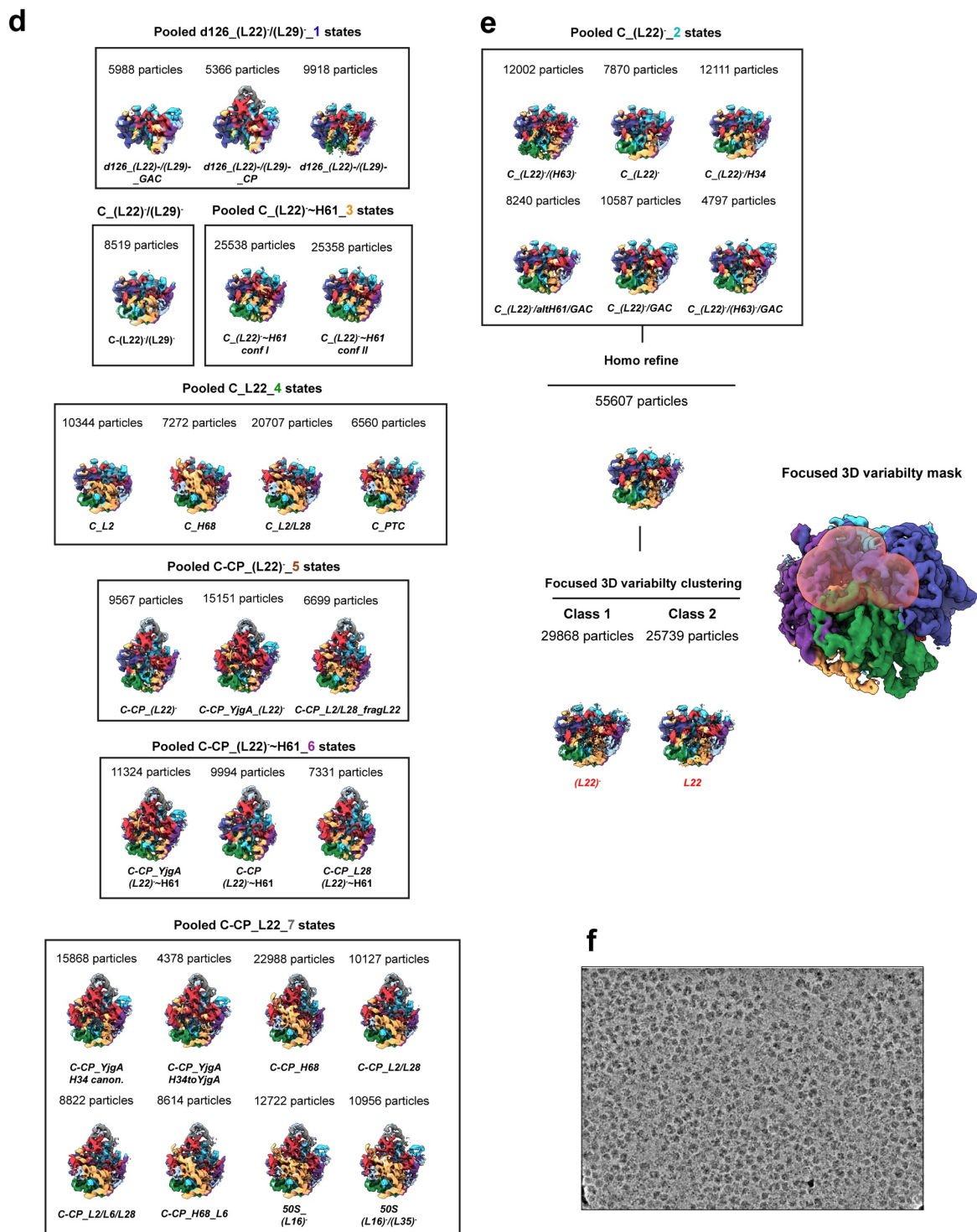
Supplementary Fig. 9 | Structures of pre-50S intermediates suggesting delayed and rerouted assembly pathways upon Api137 treatment. a Structural arrangements of identified pre-50S states 1 to 15 and 50S of the Api137-treated sample. Helix H34 and helices of domains IV and V are shown as

surface models when present in precursor states. Circles indicate the presence of the early-binding L-proteins uL22 and uL29, the intermediate-binding L-protein uL2, and the late-binding L-proteins uL16 and bL36. **b** Same as **a** but shown for control precursor states 1 to 4 and 50S. **c** Proportion of structured regions for domain IV (left) and domain V helices (right) among all precursors. Light gray: control, colored: Api137.



C

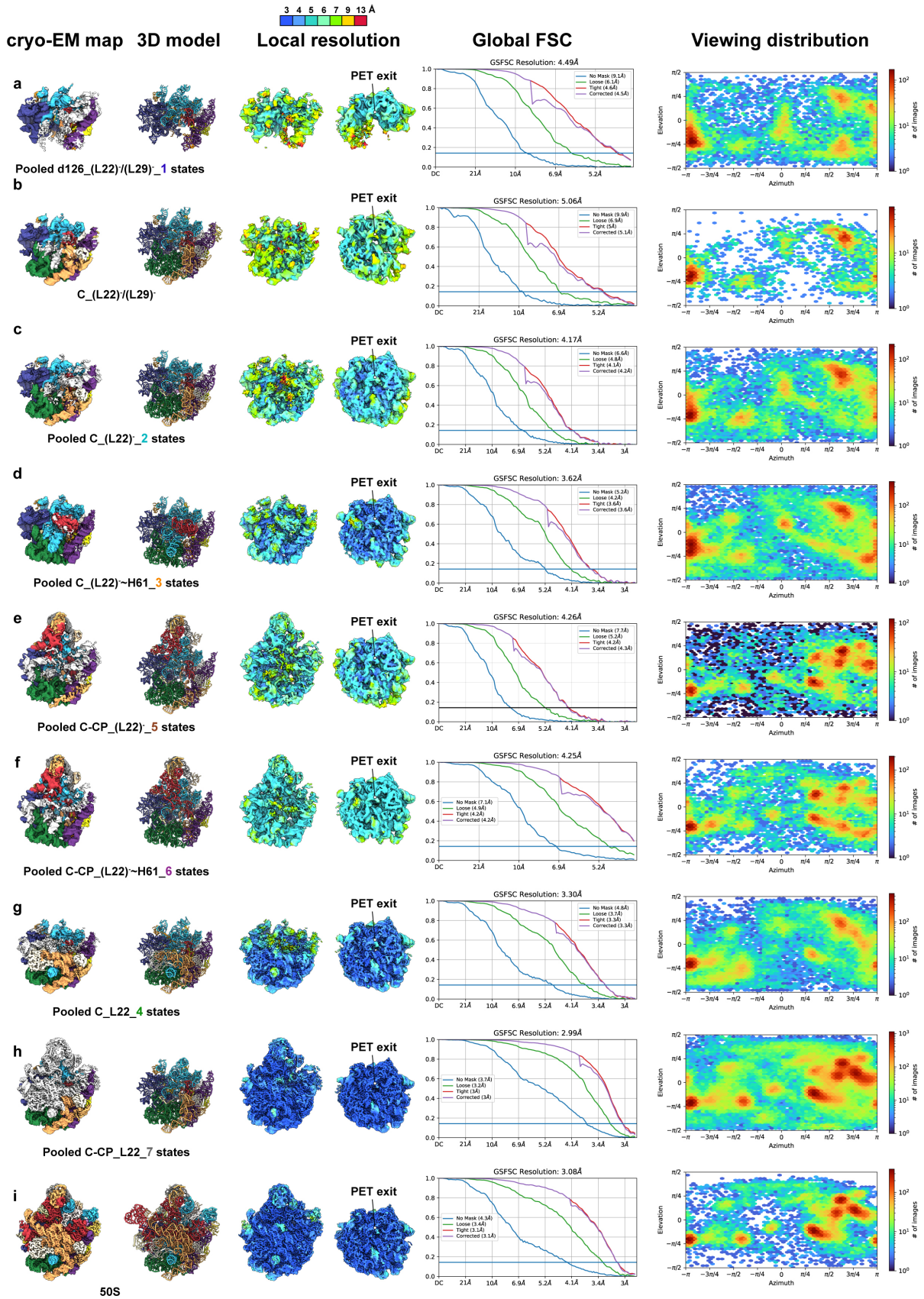




Supplementary Fig. 10 | Sorting scheme of the particles derived from Api137-treated cells supplemented with 30 μ M Api137

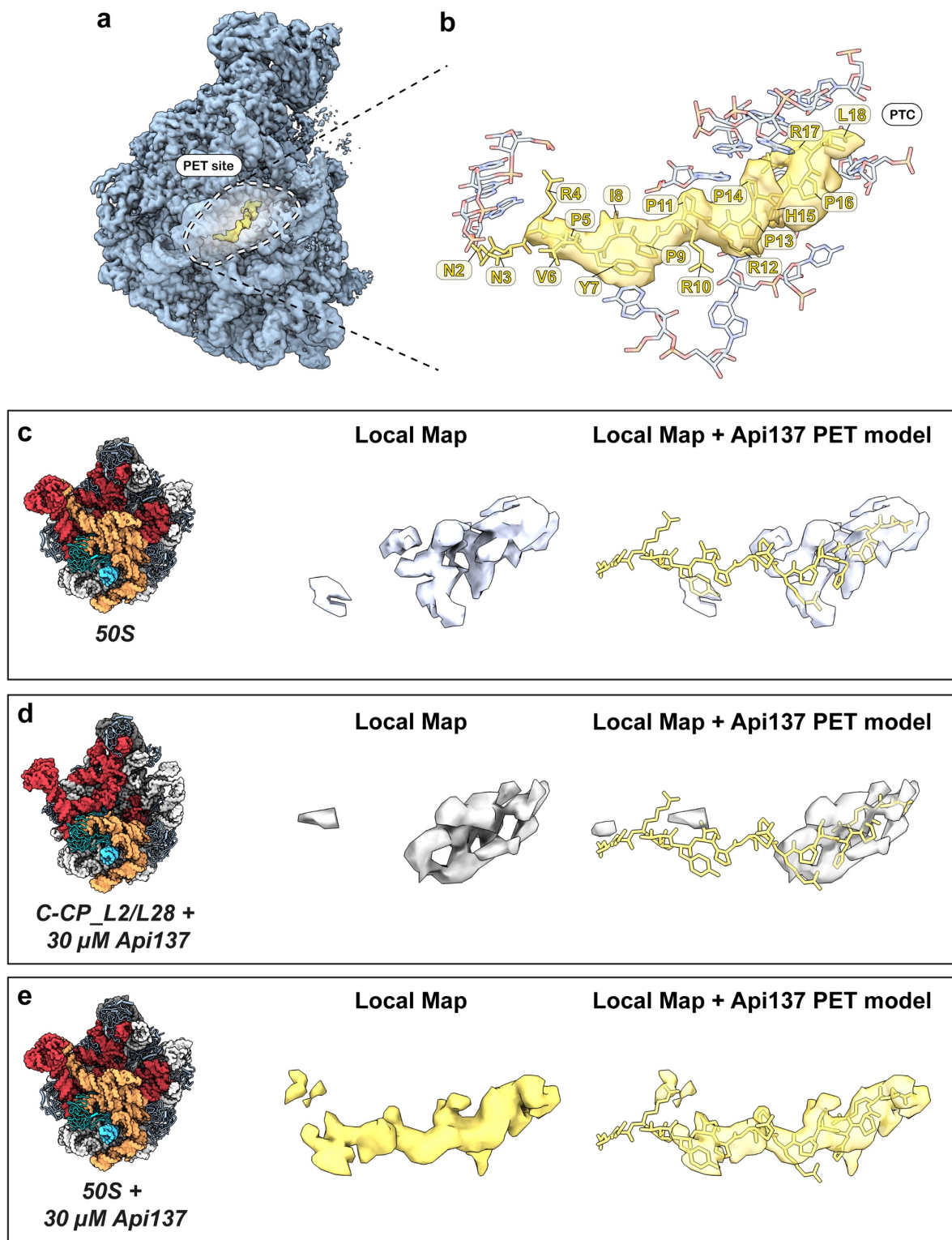
a A third data set using purified precursors from Api137-treated cells with the addition of 30 μ M Api137 was acquired. Again, generalized picking templates (see Methods) were used for template-based picking using Gautomatch. Particle images were extracted and normalized, using Relion 3.1⁴⁵ with a box size of 800 and Fourier cropped to 200 for sorting. Newly extracted particles from this data set were reassigned to the previously identified 70S, 50S, 30S and pre-50S states and non-ribosomal classes (1st

reassignment). Next, particles from the 50S, 70S and pre-50S class were reassigned to previously identified states in the first Api137 data set (2nd reassignment). Multiple classes were non-informative and were discarded after inspection by a 2D classification. Ribosomal classes were subjected to one more round of 3D variability clustering. Red asterisks indicate classes that were used for the next reassignment **b** All ribosomal particles were re-assigned to the newly identified classes (3rd reassignment). **c** Further variability was sorted using hierarchical 3D variability clustering, resulting in 30 overall pre-50S classes. Green, yellow, and purple asterisks indicate highly similar subclasses that were combined. Colored numbers next to the cryo-EM maps, indicate classes with the same arrangement of Api137 density within the PET next to the exit site. **d, e** Final classes with the same compositions at the PET exit site were pooled. **e** Classes with fragmented or absent uL22 density were pooled and subjected to another round of focused 3D variability, resulting in a (uL22)⁻ and a uL22 class. **f** Exemplary micrograph, low-pass filtered to 5 Å.



Supplementary Fig. 11 | cryo-EM maps, models, local and global resolutions and angular distributions of pooled refinements from pre-50S precursors in the presence of 30 μ M Api137. a-i Cryo-EM maps of pooled refinements (see Suppl. Figure. 10) are shown. Invariant rRNA and L-protein

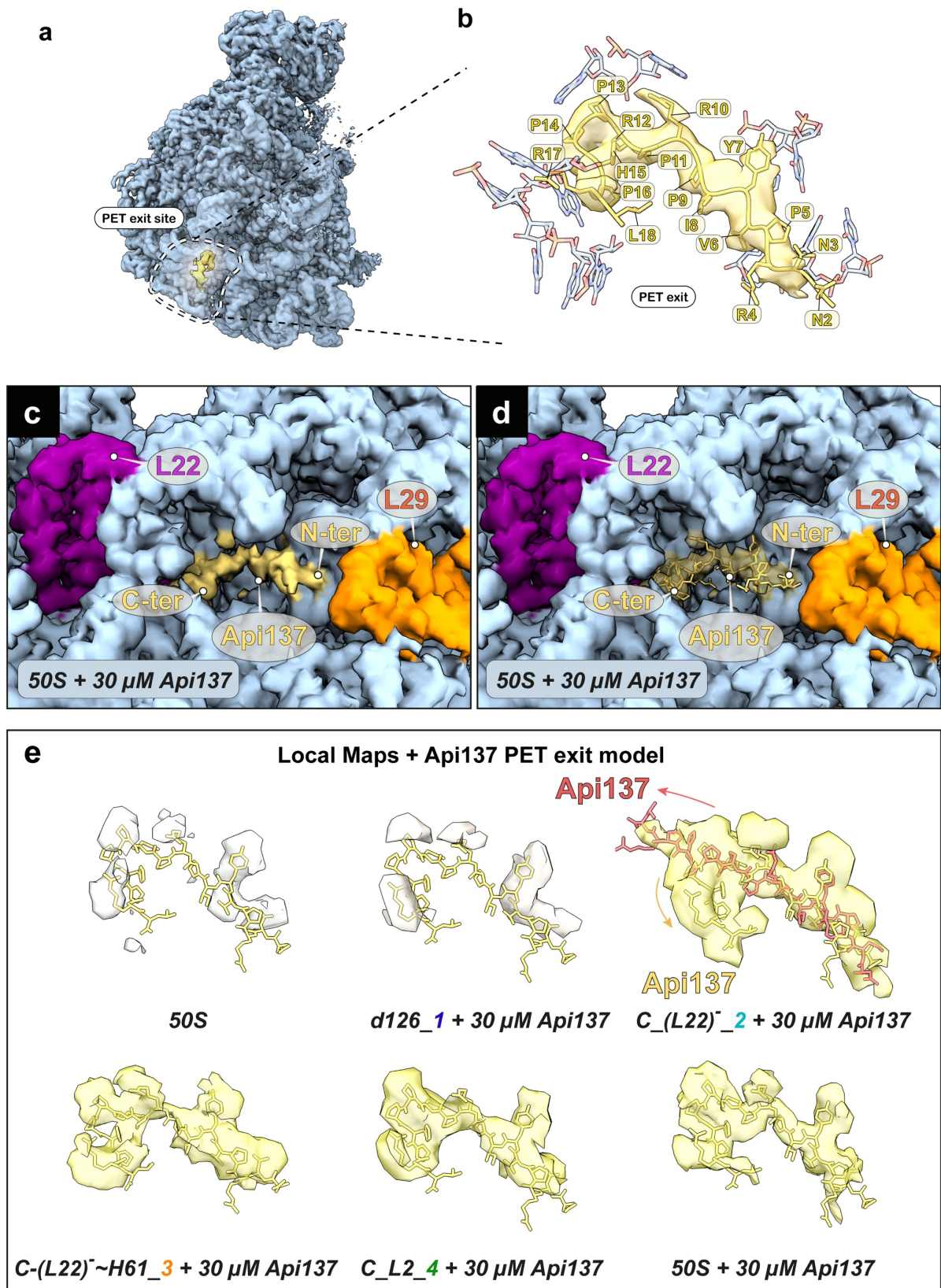
elements between individual sub-states within pooled classes are color-coded according to the six architectural domains of the 23S rRNA they are part of. Variant regions within these refinements are shown in white. PDB with invariant parts between sub-states are shown. For each state, the local resolution is shown in crown and bottom view. The Api137 PET exit bind site is indicated. Global FSC curves with estimated global resolutions at the 0.143 cut-off, as well as the angular distribution plots of the final reconstructions, are provided.



Supplementary Fig. 12 | Absence and presence of Api137 at the PET binding site

a Cryo-EM map of Api137 (yellow) bound to the 50S subunit (blue) at the PET binding site is shown. **b** Close-up of the Api137 binding site with the local density map of Api137 (transparent yellow) and the atomic model. Maps and models in **a** and **b** taken from Lauer et al., 2024 (PDB: 8RPY). **c-e** Local cryo-EM density maps for the PET binding site at a 4 Å distance from the atomic model of Api137 (rigid-body fit of PDB: 8RPY), with or without supplemented Api137. Local environments are shown

for **c** the 50S class derived from Api137-treated cells, **d** the 50S class derived from Api137-treated cells supplemented with 30 μ M Api137, and **e** the late 50S assembly precursor *C-CP_L2/L28* derived from Api137-treated cells supplemented with 30 μ M Api137. Maps were Gaussian filtered with a standard deviation of 1. Yellow-colored maps show the presence of Api137 at the PET binding site, and light grey when it is absent.



Supplementary Fig. 13 | Api137 binding to pre-50S precursors and 50S at the PET exit binding site

a Cryo-EM map of Api137 (yellow) bound to the 50S subunit (blue) at the PET exit binding site is shown. **b** Close-up of the Api137 PET exit binding site with the local density map of Api137 (transparent yellow) and the atomic model. Maps and models in **a** and **b** are taken from Lauer et al., 2024. **c, d** Cryo-EM density maps of the 50S supplemented with 30 μ M Api137 are shown. uL22 (purple), uL29 (orange), and Api137 (yellow) at its PET exit site are colored. Api137 is shown either opaque (**c**) or transparent (**d**) with the atomic model rigid-body fitted. Atomic model (PDB: 8RPY) taken from Lauer et al., 2024. **e** Local density maps for the PET exit binding site of different pooled states at a 4 Å distance from the atomic model of Api137 (rigid-body fit of PDB: 8RPY), without or with supplementation of Api137. Colored numbers indicate pooled classes with the same organizations at the PET exit site (see Supplementary Figure 10d, e). Maps were Gaussian filtered with a standard deviation of 1. Light grey cryo-EM maps indicate background, yellow-colored maps represent Api137 at the PET exit binding site.

Supplementary Table 1: Cryo-EM data collection, refinement, and validation statistics for the control data set

	#1	#2	#3	#4	#5
	<i>Ctrl_</i>	<i>Ctrl_</i>	<i>Ctrl_</i>	<i>Ctrl_</i>	<i>Ctrl_</i>
	<i>C_L2</i>	<i>C_H68</i>	<i>C-CP_L2</i>	<i>C-CP_H68</i>	<i>50S</i>
			(L22)	(L22)~H61	
Data collection and processing					
Magnification	81,000x	81,000x	81,000x	81,000x	81,000x
Voltage (kV)	300	300	300	300	300
Electron exposure (e-/Å ²)	45	45	45	45	45
Defocus range (µm)	-0.8-2.0	-0.8-2.0	-0.8-2.0	-0.8-2.0	-0.8-2.0
Pixel size (Å)	0.53	0.53	0.53	0.53	0.53
	(2.12)	(2.12)	(2.12)	(2.12)	(2.12)
Symmetry imposed	C1	C1	C1	C1	C1
Initial particle images (no.)	752,255	752,255	752,255	752,255	752,255
Final particle images (no.)	10,627	7,221	4,800	7,937	136,185
Map resolution (Å)	4.35	4.35	4.39	4.84	4.35
FSC threshold	0.143	0.143	0.143	0.143	0.143
Refinement					
Initial model used (PDB code)	8C96	8C92	8C92	8C92	6GC8
Model resolution (Å)	4.3	4.3	4.3	4.6	4.3
FSC threshold	0.143	0.143	0.143	0.143	0.143
Model resolution range (Å)	4.3-5.7	4.3-7.3	4.2-6.7	4.6-7.6	4.3-4.4
Map sharpening <i>B</i> factor (Å ²)	-62.8	-40.3	-40.3	-54.2	-62.8
Model composition					
Non-hydrogen atoms	60,216	70,943	73,704	80,332	90,280
Protein residues	1715	2,194	2,330	2,664	3,265
RNA residues	2181	2,515	2,585	2,779	3,020
<i>B</i> factors (Å²)					
Protein	-37.91	-45.36	-40.87	-138.35	-50.19
RNA	-38.84	-51.99	-64.3	-166.86	-52.14
R.m.s. deviations					
Bond lengths (Å)	0.002(0)	0.002(0)	0.005(1)	0.005(10)	0.002 (0)
Bond angles (°)	0.531(2)	0.552(4)	0.731(14)	0.551(12)	0.502(5)
Validation					
MolProbity score	1.92	1.83	1.89	2.06	1.92
Clashscore	9.25	8.56	8.31	8.48	11.14
Poor rotamers (%)	1.44	1.13	0	2.09	0
Ramachandran plot					
Favored (%)	95.53	95.36	93.24	94.86	94.89
Allowed (%)	4.35	4.55	6.68	5.14	4.99
Disallowed (%)	0.12	0.09	0.09	0	0.12

Supplementary Table 2: Cryo-EM data collection, refinement, and validation statistics for the data set from Api137-treated cells

	#1	#2	#3	#4	#5	#6	#7	#8
	<i>d126</i>	<i>C</i>	<i>C</i>	<i>C</i>	<i>C</i>	<i>C-CP</i>	<i>C-CP</i>	<i>C-CP</i>
	(<i>L29</i>) ⁻	(<i>L29</i>) ⁻	(<i>L22</i>) ⁻	(<i>L22</i>) ⁻ - <i>H61</i>	<i>GAC</i>	(<i>L22</i>) ⁻	<i>YjgA</i>	<i>YjgA</i>
	(<i>L22</i>) ⁻	(<i>L22</i>) ⁻			(<i>L22</i>) ⁻		(<i>L22</i>) ⁻ - <i>H61</i>	(<i>L22</i>) ⁻
	EMD 51828	EMD 51829	EMD 51830	EMD 51831	EMD 51832	EMD 51833	EMD 51834	EMD 51835
	PDB 9H3K	PDB 9H3L	PDB 9H3M	PDB 9H3N	PDB 9H3O	PDB 9H3P	PDB 9H3Q	PDB 93H3R
Data collection and processing								
Magnification	81,000x	81,000x	81,000x	81,000x	81,000x	81,000x	81,000x	81,000x
Voltage (kV)	300	300	300	300	300	300	300	300
Electron exposure (e ⁻ /Å ²)	45	45	45	45	45	45	45	45
Defocus range (μm)	-0.8-2.0	-0.8-2.0	-0.8-2.0	-0.8-2.0	-0.8-2.0	-0.8-2.0	-0.8-2.0	-0.8-2.0
Pixel size (Å)	0.53	0.53	0.53	0.53	0.53	0.53	0.53	0.53
	(1.41)	(1.41)	(1.41)	(1.41)	(1.41)	(2.12)	(1.41)	(1.41)
Symmetry imposed	C1	C1	C1	C1	C1	C1	C1	C1
Initial particle images (no.)	1,143,897	1,143,897	1,143,897	1,143,897	1,143,897	1,143,897	1,143,897	653,029
Final particle images (no.)	4,928	5,679	27,633	32,489	9,154	4,031	4,678	6,435
Map resolution (Å)	6.62	5.84	4.41	3.69	4.54	7.06	4.02	4.12
FSC threshold	0.143	0.143	0.143	0.143	0.143	0.143	0.143	0.143
Map resolution range (Å)	3.66-77	3.64-83	3.056-53	3.19-47	3.056-56	4.55-93	3.084-54	3.056-54
Refinement								
Initial model used (PDB code)	8C96	8C92	8C92	8C92	8C92 + 6GC8	8C90 + 6GC8	8C90 + 6GC8	8C90 + 6GC8
Model resolution (Å)	6.5	5.8	4.2	3.7	4.5	7.1	4.0	4.3
FSC threshold	0.143	0.143	0.143	0.143	0.143	0.143	0.143	0.143
Model resolution range (Å)	6.5-8.9	5.6-8.9	4.2-5.3	3.6-4.9	4.5-7.3	6.8-10.8	3.9-6.6	4.0-6.8
Map sharpening <i>B</i> factor (Å ²)	-139.5	-98	-79	-58.9	-50.9	-91.8	-24.7	-36.1
Model composition								
Non-hydrogen atoms	28,210	53,578	53,135	52,447	61,407	74,661	75,644	77,864
Protein residues	1055	1524	1464	1306	1735	2487	2,291	2526
RNA residues	1399	1946	1941	1969	2231	2573	2689	2706
<i>B</i> factors (Å ²)								
Protein	-184.13	-106.06	-108	-71.79	-100.78	-60.28	-73.85	-175.19
RNA	-233.70	-149.60	-156.98	-177.34	-157.10	-109.62	-63.63	354.94
R.m.s. deviations								
Bond lengths (Å)	0.002 (0)	0.002(4)	0.002(0)	0.002(0)	0.006(8)	0.002(4)	0.002(0)	0.002(0)
Bond angles (°)	0.500 (0)	0.637 (7)	0.490(0)	0.473(5)	0.590(14)	0.629(7)	0.505(0)	0.531(7)
Validation								
MolProbity score	1.72	1.64	1.56	1.27	2.03	1.94	1.61	1.66
Clashscore	6.71	5.51	5.45	4.95	7.62	7.28	6.41	7.51
Poor rotamers (%)	0.36	0.18	0.34	0	1.78	1.24	0.38	0.54
Ramachandran plot								
Favored (%)	94.97	95.05	96.16	97.96	93.58	92.55	96.17	96.32
Allowed (%)	4.94	4.95	3.84	2.04	6.07	7.12	3.74	3.59
Disallowed (%)	0.1	0.00	0	0.08	0.35	0.33	0.09	0.08

	#9	#10	#11	#12	#13	#14	#15	#16
	<i>C-CP</i>	<i>C</i>	<i>C</i>	<i>C-CP</i>	<i>C-CP</i>	<i>C-CP</i>	<i>50S</i>	<i>50S</i>
	<i>YfgA</i>	<i>L2</i>	<i>L2-H68</i>	<i>L2-L28</i>	<i>L2-H68</i>	<i>L2-L35-H68</i>	<i>(L16)</i>	
	EMD 51836	EMD 51837	EMD 51838	EMD 51839	EMD 51840	EMD 51841	EMD 51842	EMD 51843
	PDB 9H3S	PDB 9H3T	PDB 9H3U	PDB 9H3V	PDB 9H3W	PDB 9H3X	PDB 9H3Y	PDB 9H3Z
Data collection and processing								
Magnification	81,000x	81,000x	81,000x	81,000x	81,000x	81,000x	81,000x	81,000x
Voltage (kV)	300	300	300	300	300	300	300	300
Electron exposure (e-/Å ²)	45	45	45	45	45	45	45	45
Defocus range (µm)	-0.8-2.0	-0.8-2.0	-0.8-2.0	-0.8-2.0	-0.8-2.0	-0.8-2.0	-0.8-2.0	-0.5-2.0
Pixel size (Å)	0.53	0.53	0.53	0.53	0.53	0.53	0.53	0.53
	(2.12)	(2.12)	(2.12)	(2.12)	(2.12)	(2.12)	(2.12)	(2.12)
Symmetry imposed	C1	C1	C1	C1	C1	C1	C1	C1
Initial particle images (no.)	1,143,897	1,143,897	1,143,897	1,143,897	1,143,897	1,143,897	1,143,897	1,143,897
Final particle images (no.)	10,197	17,970	10,420	22,443	7,450	9,591	31,919	80,374
Map resolution (Å)	4.16	3.85	3.47	3.55	5.38	4.12	3.09	2.98
FSC threshold	0.143	0.143	0.143	0.143	0.143	0.143	0.143	0.143
Map resolution range (Å)	3.084-54	3.08-53	3.11-48	3.11-47	3.0-73	3.084-55	3.116-42	3.084-43
Refinement								
Initial model used (PDB code)	8C90 + 6GC8	8C91	8C91 + 6GC8	8C8Y	8C8X	6GC8	6GC8	6GC8
Model resolution (Å)	4.1	3.9	3.5	3.5	5.4	4.1	3.1	3.1
FSC threshold	0.143	0.143	0.143	0.143	0.143	0.143	0.143	0.143
Model resolution range (Å)	4.1-6.6	3.8-7.1	3.4-4.9	3.5-4.7	4.2-9.0	4.0-7.3	3.1-3.9	3.1-3.8
Map sharpening <i>B</i> factor (Å ²)	-37.2	-43.6	-25.3	-35.8	-71.7	-31.1	-36.6	-47.5
Model composition								
Non-hydrogen atoms	82,487	69,116	73,763	76,075	79,715	80,393	88,357	89,947
Protein residues	2762	2,364	2,285	2,566	2594	2708	3,036	3,222
RNA residues	2835	2,361	2,607	2,609	2769	2758	3,015	3,020
<i>B</i> factors (Å ²)								
Protein	-67.48	-41.28	-43.14	-40.59	-137.68	-138.87	-49.58	-49.21
RNA	-51.32	-46.35	51.34	65.41	-166.72	-166.61	-51.89	-52.14
R.m.s. deviations								
Bond lengths (Å)	0.002 (0)	0.002(0)	0.002(0)	0.002(0)	0.004(10)	0.004(10)	0.002(0)	0.002(0)
Bond angles (°)	0.567 (6)	0.531 (0)	0.532(2)	0.525(1)	0.534(10)	0.537(10)	0.536(0)	0.546(2)
Validation								
MolProbity score	1.61	1.57	1.62	1.67	1.72	1.7	1.60	1.55
Clashscore	5.82	5.95	5.65	5.82	6.93	6.65	5.39	5.62
Poor rotamers (%)	0.53	0.68	0.7	0.48	0.38	0.45	0.65	0.88
Ramachandran plot								
Favored (%)	95.76	96.30	95.55	94.94	95.08	95.25	95.68	96.3
Allowed (%)	4.17	3.62	4.37	5.02	4.92	4.75	4.26	3.6
Disallowed (%)	0.07	0.09	0.09	0.04	0.00	0.00	0.07	0.09

Supplementary Table 3: Cryo-EM data collection, refinement, and validation statistics for the data set from Api137-treated cells supplemented with Api137

	#1	#2	#3	#4	#5	#6	#7
	<i>Pooled</i>		<i>Pooled</i>	<i>Pooled</i>	<i>Pooled</i>	<i>Pooled</i>	<i>Pooled</i>
	<i>d126_(L29)/</i>	<i>C</i>	<i>C</i>	<i>C</i>	<i>C</i>	<i>C-CP</i>	<i>C-CP</i>
	<i>(L22)⁻</i>	<i>(L29)/</i>	<i>(L22)⁻</i>	<i>(L22)⁻</i>	<i>(L22)⁻-H61</i>	<i>(L22)⁻</i>	<i>(L22)⁻-H61</i>
		<i>(L22)⁻</i>	<i>Canonical</i>	<i>Alternative</i>			
			<i>Api137</i>	<i>Api137</i>			
	EMD xxx	EMD xxx	EMD xxx				
	PDB xxx	PDB xxx	PDB xxx				
Data collection and processing							
Magnification	81,000x	81,000x	81,000x	81,000x	81,000x	81,000x	81,000x
Voltage (kV)	300	300	300	300	300	300	300
Electron exposure (e ⁻ /Å ²)	45	45	45	45	45	45	45
Defocus range (μm)	-0.8-2.0	-0.8-2.0	-0.8-2.0	-0.8-2.0	-0.8-2.0	-0.8-2.0	-0.8-2.0
Pixel size (Å)	0.666	0.666	0.666	0.666	0.666	0.666	0.666
	(1.998)	(1.998)	(1.332)	(1.332)	(1.332)	(1.998)	(1.998)
Symmetry imposed	C1	C1	C1	C1	C1	C1	C1
Initial particle images (no.)	1,078,561	1,078,561	1,078,561	1,078,561	1,078,561	1,078,561	1,078,561
Final particle images (no.)	21,282	8,519	29,868	29,868	50,896	31,417	28,649
Map resolution (Å)	4.49	5.06	4.17	4.17	3.62	4.25	4.25
FSC threshold	0.143	0.143	0.143	0.143	0.143	0.143	0.143
Refinement							
Initial model used (this study)	<i>d126_(L29)/</i>	<i>C</i>	<i>C</i>	<i>C</i>	<i>C</i>	<i>C-CP</i>	<i>C-CP_YjgA_</i>
	<i>(L22)⁻</i>	<i>(L29)/</i>	<i>(L22)⁻</i>	<i>(L22)⁻</i>	<i>(L22)⁻-H61</i>	<i>(L22)⁻</i>	<i>(L22)⁻-H61</i>
		<i>(L22)⁻</i>					
Model resolution (Å)	6.5	5.8	4.2	4.2	3.7	4.2	4.1
FSC threshold	0.143	0.143	0.143	0.143	0.143	0.143	0.143
Model resolution range (Å)	6.5-8.9	5.6-8.9	4.2-5.3	4.2-5.3	3.6-4.9	4.0-5.6	4.0-5.6
Map sharpening <i>B</i> factor (Å ²)	-47.7	-43.9	-70.2	-70.2	-66.1	-63.2	-62.4
Model composition							
Non-hydrogen atoms	36,717	53,578	50,932	50,932	52,595	60,234	59,416
Protein residues	1055	1524	1481	1481	1323	1940	1,807
RNA residues	1329	1946	1832	1832	1969	2096	2,108
<i>B</i> factors (Å ²)							
Protein	-184.13	-106.06	-107.27	-107.27	-71.49	-59.42	-48.91
RNA	-244.21	-149.60	-151.95	-151.95	-177.34	-100.94	-47.05
R.m.s. deviations							
Bond lengths (Å)	0003 (0)	0.002(4)	0.002(0)	0.002(0)	0.002(0)	0.002(0)	0.002(0)
Bond angles (°)	0.510 (0)	0.637 (7)	0.500(0)	0.502(1)	0.478(5)	0.507(3)	0.516(0)
Validation							
MolProbity score	1.75	1.64	1.75	1.77	1.4	2.05	1.83
Clashscore	7.28	5.51	8.86	9.08	6.04	8.68	10.15
Poor rotamers (%)	0.36	0.18	0.41	0.58	0.19	1.92	0.55
Ramachandran plot							
Favored (%)	94.97	95.05	95.99	95.85	97.96	94.78	95.65
Allowed (%)	4.94	4.95	4.01	4.08	2.04	5.16	4.24
Disallowed (%)	0.1	0.00	0	0.07	0.08	0.05	0.11

	#8	#9	#10
	<i>Pooled</i>	<i>Pooled</i>	
	<i>C</i>	<i>C-CP</i>	<i>50S</i>
	<i>L2</i>	<i>L2-L28</i>	
	EMD xxx	EMD xxx	EMD xxx
	PDB xxx	PDB xxx	PDB xxx
Data collection and processing			
Magnification	81,000x	81,000x	81,000x
Voltage (kV)	300	300	300
Electron exposure (e-/Å ²)	45	45	45
Defocus range (µm)	-0.8-2.0	-0.8-2.0	-0.5-2.0
Pixel size (Å)	0.666 (1.332)	0.666 (1.332)	0.666 (1.332)
Symmetry imposed	C1	C1	C1
Initial particle images (no.)	1,078,561	1,078,561	1,078,561
Final particle images (no.)	45,271	154,257	41,476
Map resolution (Å)	3.30	2.99	3.08
FSC threshold	0.143	0.143	0.143
Refinement			
Initial model used (this study)	<i>C</i> <i>L2</i>	<i>C-CP</i> <i>L2-L28</i>	<i>50S</i>
Model resolution (Å)	3.3	3.1	3.1
FSC threshold	0.143	0.143	0.143
Model resolution range (Å)	3.1-4.1	2.8-3.3	3.1-3.8
Map sharpening <i>B</i> factor (Å ²)	-46.6	-61.3	-41.8
Model composition			
Non-hydrogen atoms	60,486	73,870	90,242
Protein residues	2,076	1,754	3,256
RNA residues	2,061	1,869	3,020
<i>B</i> factors (Å ²)			
Protein	-38.05	-26.89	-49.21
RNA	-38.20	-45.12	-52.14
R.m.s. deviations			
Bond lengths (Å)	0.002(0)	0.003(0)	0.002(0)
Bond angles (°)	0.537 (0)	0.553(4)	0.546(2)
Validation			
MolProbity score	1.79	1.75	1.55
Clashscore	9.63	6.58	5.62
Poor rotamers (%)	0.77	0.49	0.88
Ramachandran plot			
Favored (%)	95.93	94.28	96.3
Allowed (%)	3.97	5.66	3.6
Disallowed (%)	0.1	0.06	0.09